Coarsening and solidification via solvent-annealing in thin liquid films

Coarsening and solidification via solvent-annealing in thin liquid films

Tony S. Yu[1],†, Vladimir Bulović[2] and A. E. Hosoi[3]

[1]Brown School of Engineering, Brown University, Providence, RI 02906, USA

[2]Department of Electrical Engineering and Computer Science, Massachusetts Institute of Technology, Cambridge, MA 02139, USA

[3]Department of Mechanical Engineering, Massachusetts Institute of Technology, Cambridge, MA 02139, USA

We examine solidification in thin liquid films produced by annealing amorphous Alq_3 (tris-(8-hydroxyquinoline) aluminium) in methanol vapour. Micrographs acquired during annealing capture the evolution of the film: the initially-uniform film breaks up into drops that coarsen, and single crystals of Alq_3 nucleate randomly on the substrate and grow as slender 'needles'. The growth of these needles appears to follow power-law behaviour, where the growth exponent, γ, depends on the thickness of the deposited Alq_3 film. The evolution of the thin film is modelled by a lubrication equation, and an advection–diffusion equation captures the transport of Alq_3 and methanol within the film. We define a dimensionless transport parameter, α, which is analogous to an inverse Sherwood number and quantifies the relative effects of diffusion- and coarsening-driven advection. For large α-values, the model recovers the theory of one-dimensional, diffusion-driven solidification, such that $\gamma \to 1/2$. For low α-values, the collapse of drops, i.e. coarsening, drives flow and regulates the growth of needles. Within this regime, we identify two relevant limits: needles that are small compared to the typical drop size, and those that are large. Both scaling analysis and simulations of the full model reveal that $\gamma \to 2/5$ for small needles and $\gamma \to 0.29$ for large needles.

Key words: interfacial flows (free surface), low-Reynolds-number flows, lubrication theory

1. Introduction

An amorphous solid, i.e. a glass, can be 'melted' by raising its temperature above its glass-transition temperature. Alternatively, introducing solvents, or other additives, to the amorphous solid phase can reduce its glass-transition temperature below the ambient temperature, a process known as plasticization. During plasticization, the amorphous solid becomes a liquid at an ambient temperature that is above its glass-transition temperature, but below its melting temperature. Applying this process to organic semiconductors enables the growth of single crystals of organic electronics at room temperature.

† Email address for correspondence: tonysyu@brown.edu

Recent efforts to produce thin-film organic electronics have invigorated interest in the solidification of thin, liquid films. Such films have been extensively studied in the literature in the context of a wide variety of applications and physical effects (see e.g. Oron, Davis & Bankoff 1997, for a comprehensive review). These systems, often referred to as lubrication flows, share the commonality of widely disparate length scales (i.e. the film thickness compared to variations in the other dimensions). This disparity allows an asymptotic analysis in which inertial and higher-order terms of the Navier–Stokes equations are neglected, resulting in a dramatic simplification of the governing equations. Lubrication flows are particularly relevant to wet deposition (e.g. drop-casting, spin-coating; see Liu *et al.* 2009) and post-deposition annealing (Bollinne *et al.* 2003; Lee *et al.* 2004; Mascaro *et al.* 2005; Ishii *et al.* 2007; Xu, Shi & An 2008) of polymers and organic small molecules. These films can be destabilized by intermolecular forces, which can transform an initially-uniform film into drops. Over time, these drops combine to form larger drops, in a process known as coarsening (Oron *et al.* 1997; Craster & Matar 2009). Understanding the dynamics in these thin films can aid the control of film morphology, which has been shown to affect the performance of organic electronic devices (Brinkmann *et al.* 1997; Dickey, Anthony & Loo 2006; Becerril *et al.* 2008; Miller *et al.* 2008).

This desire to control film morphology has motivated numerous studies of crystallization and self-organization in thin films. For example, Rabani *et al.* (2003) observed pattern formation during the evaporation of solvent from a nano-particle solution. Using a lattice model of a nano-particle/liquid/gas system, they demonstrated qualitative agreement with the self-organization of cadmium-selenide nano-crystals from a hexane solution. In more recent work (see e.g. Náraigh & Thiffeault 2007; Naraigh & Thiffeault 2010; Thiele 2011), researchers derived a continuum model for thin films of binary fluids by combining a thin-film equation with an advection–diffusion equation. Thiele (2011) demonstrated that these models can be derived using gradient dynamics and extended this formulation to films of suspensions and to solute–solvent systems. Naraigh & Thiffeault (2010) derived a set of equations that capture the coupled effects of phase separation and free-surface variations in a thin film of binary liquid. Further analysis of this model revealed equilibrium solutions composed of extended domains in which the concentration field attained the extreme limiting values, connected by smooth transitions associated with dips in the free surface.

This paper focuses on a specific case of phase separation: long, slender crystals, i.e. needles, grown from a thin liquid film during solvent-vapour annealing (Mascaro *et al.* 2005; de Luca *et al.* 2007, 2008). In particular, Mascaro *et al.* (2005) produced extremely high-aspect-ratio Alq_3 (tris-(8-hydroxyquinoline) aluminium) needles up to a centimetre long, with characteristic cross-sectional dimensions of less than a micron. After evaporating thin (10–20 nm) films of amorphous Alq_3 onto silicon and glass substrates, Mascaro *et al.* annealed these films in a solvent vapour (chloroform or methanol) at room temperature and atmospheric pressure to promote the growth of single-crystal Alq_3 needles (similar to the needle shown in figure 1). They demonstrated that the rate of Alq_3-needle growth and its morphology depended on substrate topography, substrate properties, and solvent properties.

Motivated by Mascaro *et al.* we examine the growth of needle-like crystals from a binary fluid mixture. Through experiments, numerical modelling, and analytic scaling laws, we characterize the general growth process on planar substrates. Section 2 describes the experimental setup and annealing procedure for growing single-crystal needles from a mixture of Alq_3 and methanol. In §§ 3 and 4, the evolution of
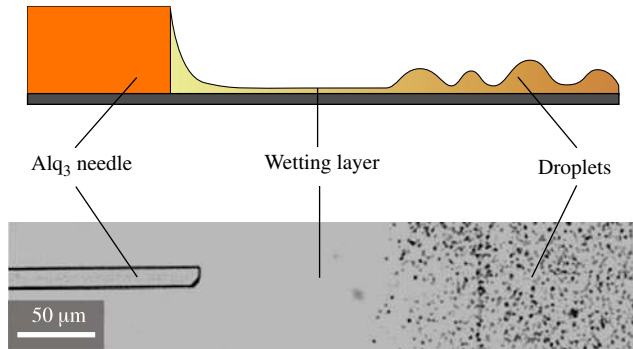
FIGURE 1. (Colour online) (*a*) Schematic of a needle growing into a fluid film. (*b*) Optical micrograph of the area surrounding an Alq$_3$ needle after annealing the Alq$_3$ film for 3 h. The rectangular needle (entering from the left of the image) is surrounded by a clear wetting layer of fluid followed by a region characterized by small droplets. Note: the schematic is drawn in a plane orthogonal to the substrate, while the micrograph shows a top-down view of the substrate.
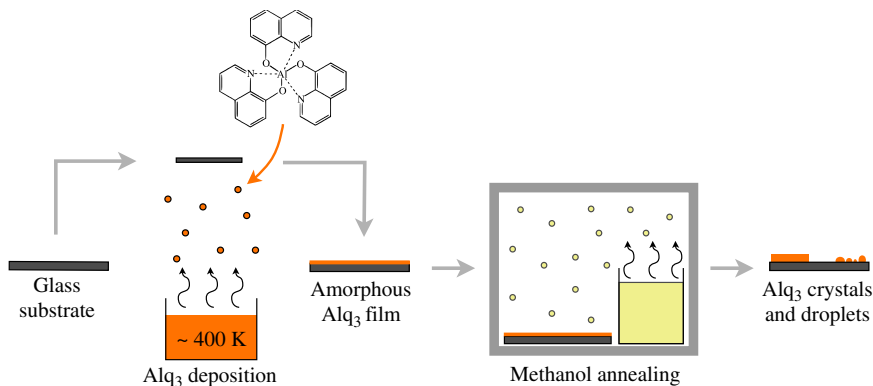

FIGURE 2. (Colour online) Growth of Alq$_3$ needles: a thin, amorphous film of Alq$_3$ is evaporated onto a half-inch-square glass substrate. The substrate is then placed in a sealed chamber along with a container of methanol. The solvent vapour fills the chamber and interacts with the Alq$_3$ film to produce droplets and needles.

the thin film is modelled by a lubrication equation, and an advection–diffusion equation captures the transport of Alq$_3$ and methanol within the film. These equations are solved numerically in §5. In §6, we derive scaling laws for the growth of needles. These scaling laws provide a physical understanding of needle growth in the diffusion-dominated and coarsening-dominated regimes. Section 7 compares the results from experiments and simulations and suggests further experiments for the interested researcher.

2. Experiments

2.1. *Experimental procedure*

The experimental procedure is outlined in figure 2. Thin, amorphous Alq$_3$ films, with film thickness H_{Alq_3} ranging between 10–60 nm, were evaporated onto half-inch-square
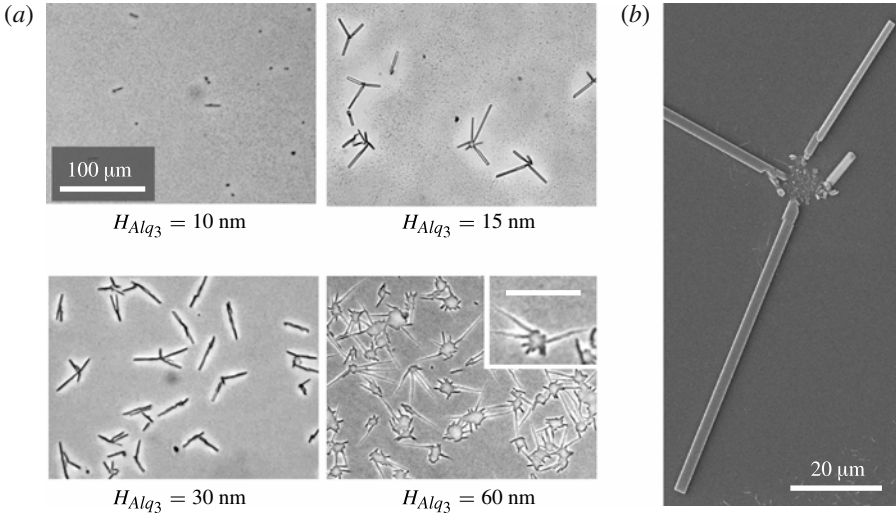
FIGURE 3. (*a*) Optical micrographs of needles for different thicknesses of Alq_3 films after annealing for 1–5 h. For $H_{Alq_3} = 60$ nm, the inset shows a magnified region with a 40 μm scale bar and a 'splotch' with tapered needles growing from its periphery. (*b*) SEM micrograph of rectangular needles growing from a common nucleation site after solvent-annealing a film with $H_{Alq_3} = 15$ nm.

glass substrates at low pressure ($\sim 10^{-6}$ Torr) with deposition rates of 1.5–2.5 Å s^{-1} (see Mascaro *et al.* 2005 for details on preparing substrates and depositing Alq_3). After deposition, a substrate, along with a container of methanol, was placed in a sealed chamber at room temperature and atmospheric pressure, for 1–5 h. During this annealing period, a small portion of the substrate (1.4 mm × 1 mm) was imaged using an optical microscope. We did not attempt to use higher-resolution imaging techniques during the annealing process (e.g. scanning electron microscopy or atomic force microscopy) because the solvent-rich atmosphere makes such imaging techniques significantly more difficult.

2.2. *Experimental results*

A few minutes into the annealing process, images of the substrate as viewed through a microscope darken, and later the substrate develops a speckled texture. This visual transformation corresponds to an initially-uniform film breaking up into small drops driven by either spinodal dewetting or hole nucleation (Lee *et al.* 2004). The first Alq_3 crystals begin to appear during this transformation. These crystal needles tend to grow in clusters surrounding a common nucleation point, as shown in figure 3. For thicker films, these points of nucleation appeared as large 'splotches' (see the micrograph for $H_{Alq_3} = 60$ nm in figure 3) that were tens of microns in diameter; the periphery of these splotches acted as nucleation sites for crystal needles. These nucleation sites were not seeded; instead, it appears they came from imperfections during deposition or, possibly, from particulate contamination during handling. It is interesting to note that the morphology and thickness dependence of these splotches resembles hole formation in nucleation-driven dewetting (see e.g. Becker *et al.* 2003). The thick rims of such holes could serve as nucleation sites, which is in agreement with our observations.
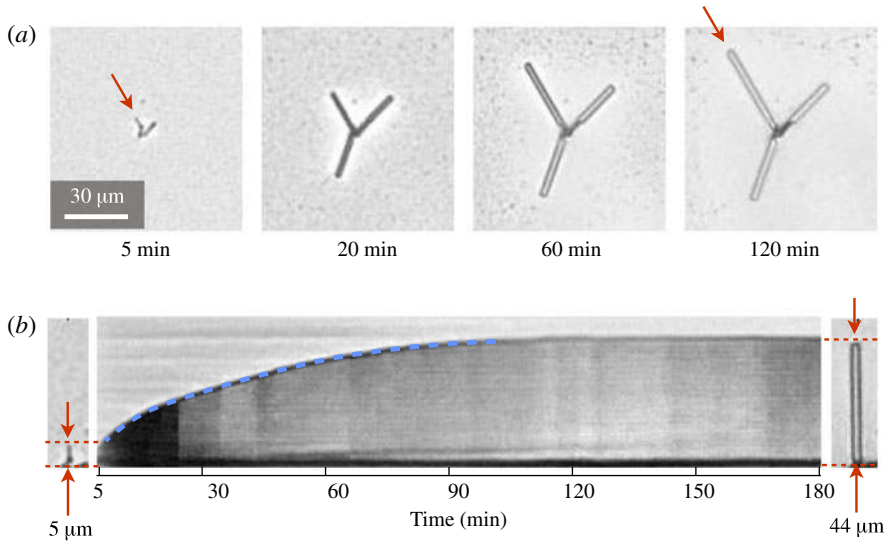
FIGURE 4. (Colour online) (*a*) Successive snapshots of a cluster of needles growing during solvent-annealing. The top-left needle from the cluster is tracked over time in (*b*). (*b*) Slice of micrograph pixels along the axis of a needle as a function of time. The line along the top of the curved shape indicates the location of the tip of the needle as a function of time and shows the needle growing from 5 to 44 μm over the course of the 3 h anneal. A dashed line highlights the position of the needle tip and ends where needle growth stops. To the left and right of the pixel-slice plot, are images of the needle 5 and 180 min into the annealing process.

In experiments, Alq_3 tends to solidify into single-crystal, high-aspect-ratio needles, as shown in the scanning electron microscope (SEM) image in figure 3(*b*). Note that Alq_3-needle formation is not specific to these experiments; needle formation is also observed in crystals grown from physical-vapour deposition (Tian *et al.* 2006) and liquid solutions of Alq_3 and solvent (Chen, Peng & Li 2008). Thus, it is likely that Alq_3 has an anisotropy in the growth due to an anisotropic surface energy, which favours needle-like morphologies (Granasy *et al.* 2004). Nevertheless, the rectangular geometry (see the SEM micrograph in figure 3*b*) breaks down for large H_{Alq_3}. The needles for $H_{Alq_3} = 60$ nm are tapered and have a sharp (as opposed to flat) tip. In addition, these tapered needles grow along slightly curved paths, in contrast to the straight paths observed in thinner films.

For rectangular needles, we track their lengths in experiments by taking a one-dimensional slice of pixels along the needle's long-axis. When sequential pixel slices are placed side-by-side, they form a simple visualization of the evolution of the needle length, as shown in figure 4. The dark curved line in figure 4(*b*) gives the position of the needle tip as a function of time and corresponds to the length of the needle, since the pixel slices start at the base of the needle.

Needle growth appeared to exhibit a power-law behaviour over one decade, such that the needle length grows like

$$L_{needle} \sim (T - T_0)^\gamma, \tag{2.1}$$

where T is time, T_0 is the time of nucleation, and γ is the growth exponent. In our experiments, T_0 was taken to be the start of the experiment. While some needles may
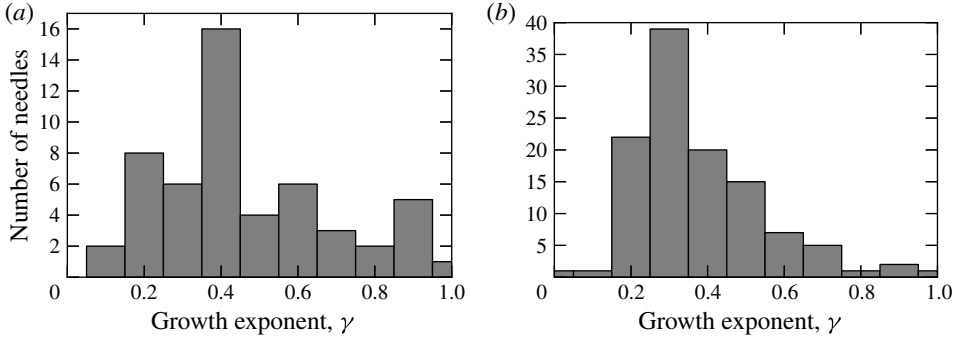
FIGURE 5. Histogram of growth exponents from solvent-annealing experiments. (*a*) 15 nm Alq$_3$ film; (*b*) 30 nm Alq$_3$ film.

nucleate at a slightly later time, we found that fitting T_0 for each needle did not have a significant impact on the long-time behaviour nor on the measured growth exponents. The dashed line in figure 4(*b*) highlights the position of the needle tip and spans the duration of this power-law regime. Needle growth slows down over time, as shown in figure 4(*b*), such that $0 < \gamma < 1$. Simulations, discussed later in this paper, suggest that this slowing of growth is due to the depletion of liquid Alq$_3$: at late times, growth saturates as nearby liquid Alq$_3$ solidifies, thus reducing the availability of mobile material.

Needles exhibited inconsistent growth exponents due to unpredictable nucleation behaviour. The randomness associated with the location, orientation, and time of nucleation can lead to needles that interfere with each other, local concentrations that are not initially uniform, and needles with different widths/thicknesses. To mitigate the influence of these growth variations, we measure the growth of many needles and look for statistically-significant growth exponents. Figure 5 compares the growth exponent, γ, for Alq$_3$ needles growing from a solvent-annealed Alq$_3$ film of thickness $H_{Alq_3} = 15$ nm and $H_{Alq_3} = 30$ nm. Despite the wide variation in the growth exponent, there are distinct peaks at $\gamma \approx 0.43$ and $\gamma \approx 0.33$ for $H_{Alq_3} = 15$ nm and $H_{Alq_3} = 30$ nm, respectively. Needles in thinner films failed to grow sufficiently long for measurement due to limited supply of Alq$_3$. In thicker films, needles were tapered and grew with slightly curved paths, as discussed earlier. These morphological differences were accompanied by irregular growth behaviour and will not be discussed further in this paper.

3. Physical picture

In these experiments, methanol vapour interacts with a solid Alq$_3$ film to produce a liquid mixture. Initially, Alq$_3$ is deposited onto glass substrates as an amorphous solid, i.e. a glass. During annealing, the presence of solvent imparts mobility to Alq$_3$ molecules and reduces its glass-transition temperature. In polymers, this reduction of the glass-transition temperature is known as plasticization (Sears & Darby 1982), a term that has also been extended to colloidal systems, where a mixture of particles of different sizes leads to an entropically-induced plasticization effect (Gotze & Voigtmann 2003). In this paper, we assume that the Alq$_3$ film has absorbed enough methanol to become liquid; thus, evolution of the Alq$_3$–methanol film is governed by the dynamics of thin liquid films. Furthermore, we neglect condensation and
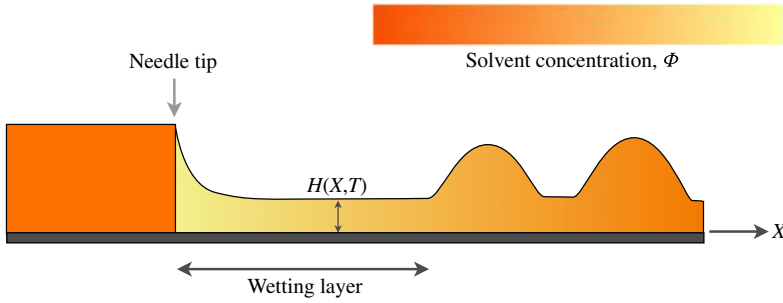
FIGURE 6. (Colour online) Schematic of a crystal needle growing in a thin, liquid film.

evaporation of solvent during needle growth. In what follows, we consider a time after a needle has nucleated from the binary mixture, as depicted in figure 6.

The mixture of Alq_3 and methanol forms a thin, liquid film with characteristic film thickness H_0 and characteristic length L in the plane of the film. (For comprehensive reviews of thin-film dynamics see Oron *et al.* 1997; Craster & Matar 2009). If $H_0 \ll L$, the lubrication approximation (see e.g. Oron *et al.* 1997) yields an evolution equation for the height, $H(X, T)$, of the fluid mixture

$$\frac{\partial H}{\partial T} = \frac{\partial}{\partial X} \left(\frac{H^3}{3\mu} \frac{\partial P}{\partial X} \right), \tag{3.1}$$

where μ is the effective viscosity of the mixture, $P(X, T)$ is the local pressure averaged over the film thickness, and X is the coordinate along the long axis of the needle. In this and all subsequent equations, we consider a one-dimensional slice of the thin film along the axis of the needle, as depicted in figure 1. Equation (3.1) is essentially an expression of mass conservation with a fluid flux $Q = -(H^3/3\mu)\partial P/\partial X$.

For films that are approximately 100 nm thick or less, intermolecular interactions between the liquid, substrate, and surrounding vapour become important. For van der Waals interactions, the interaction strength is given by the combined Hamaker constant for the solid–liquid–vapour system, A_{SLV} (Israelachvili 1991). If the van der Waals attraction is balanced by a fourth-order short-range repulsion, we can write the intermolecular pressure as

$$\Pi = \frac{A_{SLV}}{6\pi\mathscr{E}^3} \left[\left(\frac{\mathscr{E}}{H} \right)^3 - \left(\frac{\mathscr{E}}{H} \right)^4 \right], \tag{3.2}$$

where $\mathscr{E}$ is the equilibrium film thickness at which short-range repulsion balances long-range attraction. This intermolecular pressure (Sharma 1993) is also known as the disjoining pressure (Glasner & Witelski 2003), generalized disjoining pressure (Oron *et al.* 1997), disjoining–conjoining pressure (Gomba & Homsy 2009), thermomolecular pressure (Wettlaufer & Worster 2006), and Derjaguin pressure (Starov & Velarde 2009). Other exponents are commonly used in the intermolecular pressure; for example, a 3–9 pressure represents a Lennard–Jones fluid, and a 2–3 pressure represents a polar fluid. (For an overview of different contributions to the intermolecular pressure, see Teletzke, Davis & Scriven 1988.) In what follows, a 3–4 pressure is used, which is common in dewetting studies (Glasner & Witelski 2003). Note, however, that the choice of exponent does not qualitatively affect the results presented in this paper. The choice of pressure exponents controls the time constant

for the dewetting instability, but the power-law behaviour described in the following sections applies only after dewetting. In particular, note that the scaling analysis presented in §6 is not influenced by the exponents in Π.

In addition to the intermolecular pressure, surface tension, σ, produces a pressure jump across a curved liquid/vapour interface; thus, the total fluid pressure is

$$P(X, T) = -\sigma \frac{\partial^2 H}{\partial X^2} + \Pi(H). \tag{3.3}$$

The competition between surface tension and intermolecular forces causes the initially-uniform film to break up into drops through either spinodal or nucleation-driven dewetting (Lee *et al.* 2004). Note that the short-range repulsive force in Π prevents the formation of dry spots; i.e. repulsion prevents $H \to 0$. Although the term 'dewetting' suggests complete removal of fluid, here and in the literature (see e.g. Becker *et al.* 2003; Glasner & Witelski 2003; Craster & Matar 2009), it describes the progression toward an ultra-thin film ($H \approx \mathcal{E}$) rather than film rupture. After dewetting, the drops coarsen, during which capillary pressure dominates in drops, while intermolecular pressure dominates in the ultra-thin film forming a slowly-evolving, quasi-steady configuration. In this paper, we assume that drop formation is driven by spinodal dewetting. Although this assumption will affect the dewetting dynamics in simulations (e.g. the dewetting time scale), it will not significantly influence coarsening behaviour, which is the focus of this paper.

In our system, the fluid film is composed of a binary mixture of Alq_3 and solvent molecules; hence, a second equation is required to track motion of solvent relative to the mixture. The composition of the film is characterized by a local solvent concentration, $\Phi(X, T)$, which is averaged over the film thickness. It is important to emphasize that we write these equations in terms of the solvent concentration, not the solute concentration, as is common in much of the literature (see e.g. Thiele 2011). Solvent is advected by fluid flow and driven down concentration gradients by diffusion. Combining these effects leads to an advection–diffusion equation describing the transport of solvent:

$$\frac{\partial(\Phi H)}{\partial T} = \frac{\partial}{\partial X} \left(\Phi \frac{H^3}{3\mu} \frac{\partial P}{\partial X} + DH \frac{\partial \Phi}{\partial X} \right), \tag{3.4}$$

where D is the diffusivity of solvent in the mixture. The first term on the right-hand side describes solvent that is advected with the flow (see e.g. Zhou *et al.* 2005; Cook, Bertozzi & Hosoi 2008), and the second term describes transport of solvent relative to the mixture via diffusion. Note that Φ is the volume fraction of solvent averaged over the film thickness, and we neglect variations of volume with concentration, as reflected in (3.4). Thus, the diffusion term does not produce net mass flux, which is consistent with the absence of a diffusion term in (3.1). Furthermore, we have assumed that all material properties are independent of concentration in order to make the model tractable. This assumption implies that the system is far from the glass transition, since material properties will vary rapidly with small changes in concentration near the glass transition.

During the deposition process, the Alq_3 film is frozen into a metastable, glassy state (Mascaro *et al.* 2005). After plasticization, Alq_3 molecules are free to crystallize. At the solid/liquid interface of a growing crystal needle, we assume local equilibrium at the needle tip (Langer 1980; Balluffi, Allen & Carter 2005), such that the solvent concentrations at the tip are fixed at Φ_{solid} and Φ_{tip} on the solid and liquid sides of the

Dimensionless parameter	Symbol	Definition	Order of magnitude
Surface tension	$\mathscr{S}$	$\dfrac{\rho \sigma H_0^4}{3\mu^2 L^3}$	10^{-8}
Intermolecular attraction	$\mathscr{A}$	$\dfrac{\rho A_{SLV} H_0^3}{18\pi\mu^2 \mathscr{E}^3 L}$	10^{-6}
Diffusivity	$\mathscr{D}$	$\dfrac{\rho D H_0}{\mu L}$	10^{-6}
Transport coefficient	$\alpha = \dfrac{\mathscr{D}}{\mathscr{A}}$	$\dfrac{18\pi\mu D\mathscr{E}^3}{A_{SLV} H_0^2}$	1

TABLE 1. Relevant dimensionless groups for the binary thin film. These values are estimated using values for pure methanol with density $\rho = 0.8$ g cm^{-3} and viscosity $\mu = 5 \times 10^{-4}$ Pa s^1. The diffusivity, $D = 0.4$ cm^2 s^{-1}, is estimated by considering an Alq$_3$ molecule in pure methanol. A glass/methanol/air system provides an estimate of the Hamaker constant $A_{123} = 10^{-20}$ kg m^2 s^{-2}. Length scales of $L = 10$ μm and $H_0 = 10$ nm are estimated from experiments.

interface, respectively. These fixed values provide the relevant boundary condition at the needle tip if solidification is limited by transport of Alq$_3$, not by interface kinetics. Under these conditions, growth of the needle is limited by transport of Alq$_3$ to the needle; thus, the needle-tip velocity, V_{tip}, is given by the Stefan condition for moving boundaries (Langer 1980):

$$V_{tip} = \frac{\partial X_{tip}}{\partial T} = \frac{D}{\Phi_{solid} - \Phi_{tip}} \frac{\partial \Phi}{\partial X}\bigg|_{tip}. \tag{3.5}$$

Here, Φ_{solid} is small (Alq$_3$-rich), and Φ_{tip} is comparatively large (solvent-rich), such that the needle grows in the opposite direction to the concentration gradient.

4. Mathematical model

Before developing a dimensionless mathematical model, we define an initial film thickness H_0, a characteristic horizontal length L, and characteristic time scale $T_0 = \rho H_0 L/\mu$. Using these length and time scales, we define the dimensionless parameters

$$\mathscr{S} = \frac{\rho \sigma H_0^4}{3\mu^2 L^3}, \tag{4.1}$$

$$\mathscr{A} = \frac{\rho A_{SLV} H_0^3}{18\pi\mu^2 \mathscr{E}^3 L}, \tag{4.2}$$

$$\mathscr{D} = \frac{\rho D H_0}{\mu L}, \tag{4.3}$$

which measure the magnitude of surface tension, intermolecular interactions, and diffusivity relative to viscous effects (see table 1). Note that $\mathscr{S}$ and $\mathscr{D}$ are proportional to an inverse capillary number and an inverse Schmidt number (i.e. mass-transfer Prandtl number), respectively.

Following the work of Kao, Golovin & Davis (2006), we rescale X and T by dimensionless length and time scales proportional to the most unstable wavelength and characteristic time:

$$x = \sqrt{\frac{\mathscr{A}}{\mathscr{S}}} \frac{X}{L}, \qquad t = \frac{\mathscr{A}^2}{\mathscr{S}} \frac{T}{\rho H_0 L / \mu}. \qquad (4.4)$$

This scaling reduces the governing equations, (3.1), (3.4) and (3.3), into dimensionless form:

$$\frac{\partial h}{\partial t} = \frac{\partial}{\partial x} \left(h^3 \frac{\partial p}{\partial x} \right), \qquad (4.5a)$$

$$\frac{\partial \phi h}{\partial t} = \frac{\partial}{\partial x} \left(\alpha h \frac{\partial \phi}{\partial x} + \phi h^3 \frac{\partial p}{\partial x} \right), \qquad (4.5b)$$

$$p = -\frac{\partial^2 h}{\partial x^2} + \left[\left(\frac{\varepsilon}{h} \right)^3 - \left(\frac{\varepsilon}{h} \right)^4 \right]. \qquad (4.5c)$$

The only remaining parameters in these equations are $\varepsilon = \mathscr{E}/H_0$ (the dimensionless equilibrium film thickness) and

$$\alpha = \frac{\mathscr{D}}{\mathscr{A}}, \qquad (4.6)$$

a dimensionless transport parameter relating the speed of diffusion to the speed of advection driven by the collapse of drops, i.e. coarsening, which, itself, is driven by the strength of intermolecular attraction. For high values of α, diffusion dominates; in contrast, advection due to coarsening dominates at low α-values. Thus, this transport parameter is analogous to an inverse Sherwood number or mass-transfer Nusselt number.

The needle velocity in (3.5) is rescaled by substitution of the rescaled length and time from (4.4), such that

$$v_{tip} = -\alpha \frac{\partial \phi}{\partial x} \bigg|_{tip}. \qquad (4.7)$$

Note that the solvent concentration above, and in (4.5b), is expressed in dimensionless terms as

$$\phi = \frac{\Phi - \Phi_{solid}}{\Phi_{tip} - \Phi_{solid}}. \qquad (4.8)$$

This rescaling fixes $\phi_{solid} = 0$ and $\phi_{tip} = 1$, such that $\phi_{solid} - \phi_{tip} = -1$ when rewriting (3.5) as (4.7). The governing equations, given by (4.5), combined with the boundary condition at the needle tip (equation (4.7)), constitute the mathematical model for the thin-film mixture of Alq_3 and solvent.

5. Numerical results

5.1. *Numerical details*

The governing equations given by (4.5) were solved numerically using centred finite differences and fully-implicit time steps (Press *et al.* 1992). Note that the concentration is decoupled from the film thickness in (4.5), such that ϕ can be solved after solving for h at each time step. An adaptive proportional–integral–derivative (PID) control scheme (Valli, Carey & Coutinho 2005) varied the time steps to minimize run time.
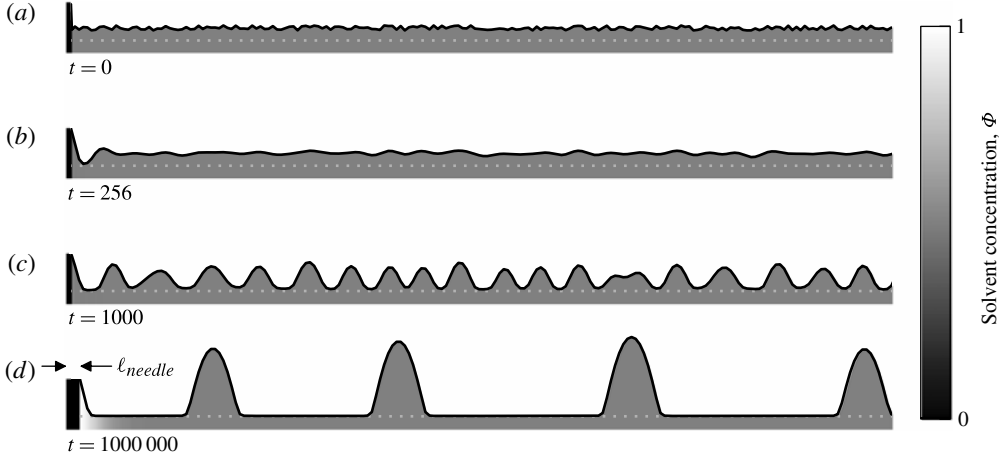
FIGURE 7. Evolving thin film. A solid needle grows from the left. At $t = 0$, (a), the fluid film has a uniform, but rough, thickness. At a characteristic time (here at $t = 256$, b) the uniform film becomes unstable and breaks up into small drops ($t = 1000$, c). At late times, (d), drops collapse and coalesce to form larger, more coarsely-spaced drops. The grey dotted line indicates the equilibrium ultra-thin-film thickness.

At each time step, the system was solved using a two-step procedure: first we solved for h and ϕ using (4.5), while holding the needle tip fixed; next, we advanced the needle tip using (4.7). During the solution of (4.5), no-flux boundary conditions were enforced at both edges of the fluid domain (i.e. the right edge of figure 7 and at the tip of the needle on the left side). At the boundary opposite the needle tip, no flux is equivalent to a symmetry boundary condition with zero first- and third-derivatives of the film thickness, h (as described in Glasner & Witelski 2003). At the needle tip, this no-flux boundary condition was modified to account for the mesh spacing that was deformed by the needle tip (see Yu 2011, for details). The fluid was assumed to wet the tip of the needle, such that the height on the solid and liquid sides of the tip are equal; i.e. $h_{tip} = h_{solid}$, where the subscript 'tip' denotes values on the liquid side of the needle tip. After solving (4.5) with no-flux boundary conditions, the needle tip was advanced using (4.7), and the concentration on the solid and liquid sides of the needle tip were fixed at ϕ_{solid} and ϕ_{tip}. Thus, the needle tip switches from a no-flux boundary to an absorbing boundary, during which solute was removed from the fluid domain and added to the needle. This mass transfer increases the needle length and reduces both the length of the fluid domain and the fluid height, since the needle is taller than the nearby fluid.

The main parameters of the simulation are the dimensionless equilibrium film thickness (ε), the initial concentration of the fluid (ϕ_0), the height of the needle (h_{solid}), and the transport parameter (α). In the following simulation results, $\varepsilon = 0.5$, $\phi_0 = 0.5$, $2 < h_{solid} < 64$, and $10^{-4} < \alpha < 10^1$. Note that varying ϕ_0 alters the magnitude of the tip velocity, but it does not affect the growth exponent of the needle. Furthermore, varying ε alters the characteristic time for dewetting, but the growth exponent measured after dewetting is unchanged. These details are discussed further in Yu (2011).
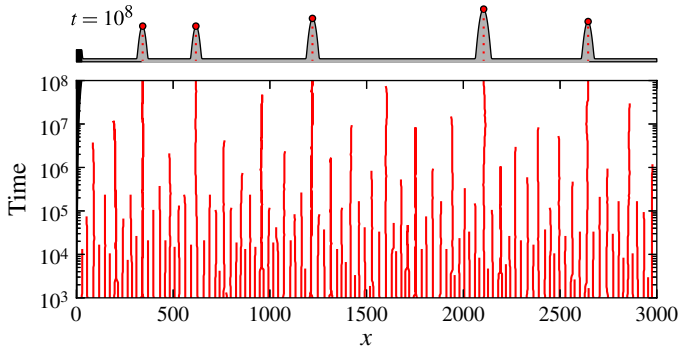
FIGURE 8. (Colour online) Evolution of drop positions during coarsening. Each line in the bottom plot denotes the position of a drop centre as a function of time. The termination of a line coincides with the collapse of a drop. The schematic at the top denotes the thin-film profile at $t = 10^8$ with the drop centres highlighted by dots.

5.2. *Observed phenomena*

At the start of simulations, a seed of solid Alq_3 is placed at the left edge of the domain to nucleate the crystal, as shown in figure 7(*a*). Solvent concentration in the fluid domain is initialized with a uniform value (i.e. $\phi_0 = $ constant for $x > x_{tip}$), and the thin-film thickness is initialized as $h_0 = 1 + \delta(x)$, where $\delta(x)$ adds uniform noise with an amplitude of approximately 1/10th of the initial film thickness. This magnitude is comparable to the expected roughness of the thin film in experiments.

At early times, surface tension smooths the initially-rough film, as shown at $t = 256$ in figure 7(*b*). After this initial smoothing, the competition between intermolecular forces and surface tension drives the formation of drops, as shown on the right side of figure 1. From linear stability analysis (see Craster & Matar 2009, for an overview), we can calculate the dimensionless characteristic time and wavelength for this instability:

$$\tau_{dewet} = \frac{4}{(3\varepsilon^3 - 4\varepsilon^4)^2}, \tag{5.1}$$

$$\lambda_{dewet} = 2\pi\sqrt{\frac{2}{(3\varepsilon^3 - 4\varepsilon^4)}}. \tag{5.2}$$

The simplicity of these relations is due to the fact that the dimensionless parameters in (4.4) were based on this stability analysis. Equations (5.1) and (5.2) tell us that the initially-uniform film is unstable to perturbations when $\varepsilon < 3/4$. For all simulations in this paper, $\varepsilon = 0.5$ such that the characteristic time for instability is $\tau_{dewet} = 256$. The undulations in the film at τ_{dewet} lead to the formation of drops by $t = 1000$. At late times, drops collapse and coalesce to form larger, more coarsely-spaced drops (figure 7*d*). This coarsening process is visualized in figure 8, which shows the position of drop centres over time. The abrupt termination of drop centres reflects the fact that drops do not collide during coarsening. Instead, a collapsing drop pushes fluid through the ultra-thin film to adjacent drops (Glasner & Witelski 2003, 2005). During this transformation, the needle grows from the left edge of the domain. Since the needle is Alq_3-rich, the fluid near the needle tip becomes solvent-rich as shown in figure 7(*d*).
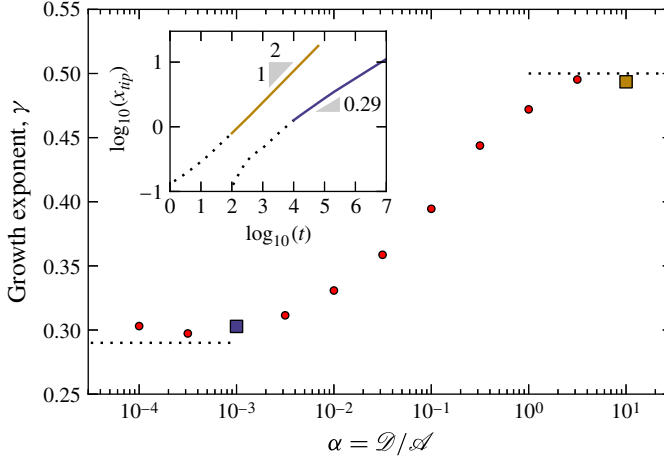
FIGURE 9. (Colour online) Growth rate as a function of α. At high α, diffusion dominates and the growth rate approaches $t^{1/2}$. At low α, coarsening dominates and the growth rate approaches $t^{0.29}$. Inset: log–log plot of x_{tip} (needle length) as a function of time for low α (10^{-3}; lower curve) and high α (10; upper curve). The dotted curves correspond to growth transients. The upper and lower curves in the inset correspond to the upper and lower square markers in the main plot.

In the numerical model, we have assumed that fluid wets the needle such that a meniscus forms at the needle tip. When the needle height is larger than the typical drop height, then the pressure in the meniscus will be lower than the pressure in the film. This pressure difference drives flow toward the needle tip and promotes the collapse of drops near the tip. Higher rates of drop collapse lead to a larger-than-typical separation between the needle tip and the nearest drop. In this paper, this separation is called the wetting layer, which is shown schematically in figure 11 (denoted by ℓ_{wet}). These wetting layers match the clear regions surrounding needles in experiments, as shown in figure 4. Note that no wetting layer is present in figure 7 because the drop heights are always comparable to or larger than the needle height in this simulation.

5.3. *Needle growth*

The growth of needles is captured by the growth exponent, γ, where $\ell_{needle} = L_{needle}/L \sim t^{\gamma}$. Note that ℓ_{needle} is equivalent to x_{tip} since the needle grows from the origin. Simulation results shown in figure 9 indicate that γ grows monotonically with the transport parameter, α. The simulation data in figure 9 focus on needle growth during an intermediate time range. At early times, simulations display a transient growth (see the lower curve in the inset of figure 9). This transient is a numerical artifact, due to finite spatial resolution, that lasts until the diffusion front grows beyond the first few mesh points and has a characteristic time $\tau_{numerical} \sim \Delta x^2/4\alpha$ (see Yu 2011, C.2.2 for more details). Furthermore, the dewetting process, with characteristic time τ_{dewet}, also alters needle growth. The growth exponents reported here are measured after these transients. In addition, two late-time effects are ignored: (i) when all drops have collapsed, the dynamics change since droplet collapse can no longer feed the needle, and (ii) when the diffusive front at the growing needle tip

reaches the no-flux boundary opposite the needle, needle growth slows. This boundary effect is analogous to the saturation of needle growth in experiments.

In addition to the late-time transients discussed above, we encounter an additional difficulty when drops grow much larger than the needle. When drops are small compared to the needle, the collapse of an individual drop has only a minor effect on needle growth, and the average of many drop collapses governs needle growth via advection. As time progresses, however, the film coarsens such that drops can grow larger than the needle, and each droplet collapse near the needle tip noticeably perturbs the growth rate of the needle resulting in discontinuities that increase in magnitude and rarity as time progresses. These late-time dynamics are not analysed in the following scaling analysis which assumes a continuous growth rate of the needle.

6. Needle growth regimes

The simulation results in figure 9 suggest asymptotes to true power laws in γ for high and low values of α that are connected by a cross-over regime for moderate values of α. In the following, we derive asymptotic values of γ for diffusion-dominated and coarsening-dominated regimes.

6.1. *High α-values: diffusion-dominated needle growth*

For high α-values, transport via diffusion dominates: solvent diffuses through the liquid faster than advection can carry it. Thus, in the high-α limit, this system reduces to the problem of one-dimensional diffusion,

$$\frac{\partial \phi}{\partial t} = \alpha \frac{\partial^2 \phi}{\partial x^2}, \tag{6.1}$$

which, for an infinite domain, can be solved by a similarity solution (see e.g. Crank 1975). The one-dimensional diffusion equation with a Stefan boundary condition, i.e. (4.7), yields an expression for the dimensionless needle length: $\ell_{needle} \sim t^{1/2}$.

6.2. *Low α-values: coarsening-dominated needle growth*

Coarsening causes drops to collapse and drives flow through the liquid film. For low α-values, this flow carries solvent through the film faster than diffusion. Near the needle tip, collapsing drops drive fluid toward the needle tip. However, not all of that fluid can be incorporated into the needle since it has a specific composition, i.e. ϕ_{solid}. Since the needle is solvent-poor, left-over solvent builds up in front of the needle tip and slows down needle growth. Thus, the needle growth rate depends on the local solvent concentration. This concentration is governed by diffusion, the flux of fluid toward the needle tip, and the rejection of solvent at the needle tip, which is a local source of solvent.

In simulations, the needle length scales like a power law in time. To that end, we seek solutions in which the meniscus length, ℓ_m, and the difference in concentration between the needle tip and meniscus edge, $\Delta\phi = \phi_{tip} - \phi_m$, change like power laws:

$$\ell_m \sim t^a, \quad \Delta\phi \sim t^{-b}, \tag{6.2}$$

where exponents a and b are positive. As solvent builds up in front of the needle, ϕ_m asymptotically approaches ϕ_{tip}, such that $\Delta\phi \to 0$; this leads to a decaying power law, as suggested by the negative exponent. Furthermore, we expect these variables to asymptote, such that their exponents should be less than 1.
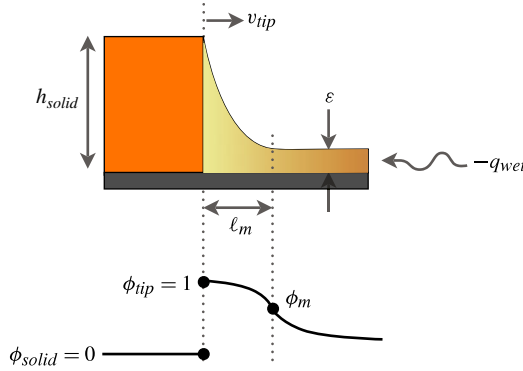
FIGURE 10. (Colour online) A meniscus connects the needle tip to a thin wetting layer with approximate thickness ε. Fluid flux across the right edge of the meniscus, x_m, is given by q_{wet}. On the left edge, Alq_3 leaves the meniscus as it solidifies into the solid crystal needle.

To solve for the velocity of the needle, we apply mass conservation of the mixture on a control volume around the needle tip, as shown in figure 10. At low α-values, mass consumed by the growing needle must balance the fluid flux through the wetting layer and the mass change in the meniscus. Thus, the mass balance around the moving control volume in figure 10 can be written as

$$v_{tip}\, h_{solid} + \dot{\mathcal{V}}_m = -q_{\text{wet}} + v_{tip}\, \varepsilon, \tag{6.3}$$

where q_{wet} is the flux through the wetting layer, v_{tip} is the needle velocity, and $\dot{\mathcal{V}}_m$ is the time derivative of the fluid volume in the meniscus. Here, q_{wet} can vary in time, but it is spatially invariant because $h \approx \varepsilon$ in the wetting layer. The needle velocity adds to the flux because we take a reference frame that moves with the needle tip.

The needle velocity given by (4.7), can be approximated as

$$v_{tip} \approx -\alpha \frac{\phi_m - \phi_{tip}}{\ell_m} \sim \frac{\Delta\phi}{\ell_m} \sim t^{-a-b}. \tag{6.4}$$

Since a and b are positive, (6.4) suggests that the velocity slows over time.

To approximate the volume of the meniscus in (6.3), we first focus on the shape of the meniscus. When the height at the needle tip is large, the majority of the meniscus is much higher than the equilibrium thin-film height, ε. Thus, surface-tension effects dominate intermolecular forces and the meniscus is roughly parabolic:

$$h \sim h_{solid} \left(\frac{x}{\ell_m} \right)^2. \tag{6.5}$$

This shape gives a meniscus volume with a time rate of change

$$\dot{\mathcal{V}}_m = \frac{\mathrm{d}}{\mathrm{d}t} \int_{\ell_m} h\,\mathrm{d}x \sim h_{solid}\,\dot{\ell}_m \sim t^{a-1}. \tag{6.6}$$

The flux in (6.3) is driven by pressure differences between the meniscus and the nearest drop. The meniscus at the needle tip creates a low-pressure region (because $\partial^2 h/\partial x^2 > 0$), while the curvature of the drop closest to the needle tip, i.e. the first drop, creates a high-pressure region (because $\partial^2 h/\partial x^2 < 0$). The resulting flow through
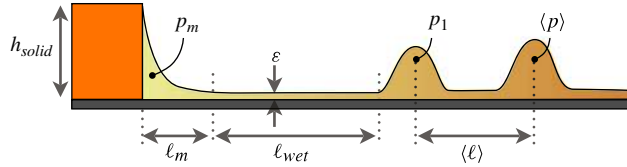
FIGURE 11. (Colour online) Schematic of needle growing from left to right. A meniscus, with pressure p_m, connects the needle tip and a thin wetting layer. Fluid flow to the needle is driven by the pressure difference between the meniscus and the drop closest to the needle tip, i.e. the first drop.

the wetting layer is

$$q_{\text{wet}} = -h^3 \frac{\partial p}{\partial x} \sim -\varepsilon^3 \frac{p_1 - p_m}{\ell_{\text{wet}}}, \tag{6.7}$$

where p_1 is the pressure of the first drop, and ℓ_{wet} is the length of the wetting layer as shown in figure 11. The scaling for this flux depends on the height of the needle and will be discussed in the following sections.

6.3. *Needle growth for low α-values and small h_{solid}*

When the height of the needle, h_{solid}, is roughly the same size as (or smaller than) the typical drop, we say the needle is small. In this limit, the pressure in the meniscus is comparable to that of the typical drop, $\langle p \rangle$, and the distance from the needle tip to the first drop is comparable to the typical drop spacing, $\langle \ell \rangle$; thus, the flux through the film, given by (6.7), simplifies to $q_{\text{wet}} \sim -\varepsilon^3 \langle p \rangle / \langle \ell \rangle$. This calculation is identical to that in Glasner & Witelski (2003), in which they compute that the typical drop pressure and drop spacing for coarsening films scale as $\langle p \rangle \sim t^{-1/5}$ and $\langle \ell \rangle \sim t^{2/5}$, such that

$$q_{\text{wet}} \sim t^{-3/5}. \tag{6.8}$$

To solve for the needle velocity, we note that moderate meniscus pressures correspond to meniscus lengths that are insensitive to pressure variations (see (6.12) below). Thus, the change in meniscus volume is negligible in this small-h_{solid} regime, and (6.3) simplifies to

$$v_{tip} \sim q_{\text{wet}} \sim t^{-3/5}. \tag{6.9}$$

Integrating once in time gives a needle length that scales as

$$\ell_{needle} \sim t^{2/5}. \tag{6.10}$$

Figure 12 compares this asymptotic limit for ℓ_{needle} to simulation results. As h_{solid} approaches 1 (the initial thin-film thickness), the growth exponent approaches 2/5, as predicted.

6.4. *Needle growth for low α-values and large h_{solid}*

When the needle height is much larger than the typical drop height, we say that the needle is large. For large needles, the pressure in the meniscus region is large in magnitude, i.e. $|p_m| \gg |\langle p \rangle|$, such that (6.7) becomes

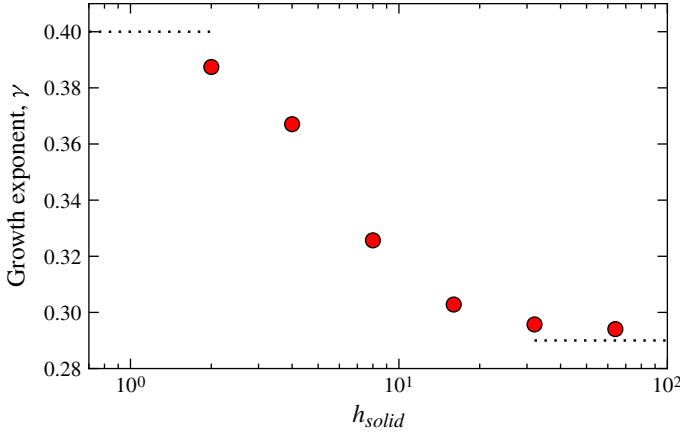$$q_{\text{wet}} \sim \varepsilon^3 p_m / \ell_{\text{wet}}. \tag{6.11}$$

FIGURE 12. (Colour online) Growth rate as a function of the height of the needle, h_{solid}.

Before deriving a scaling law for flux through the wetting layer, we first derive scaling laws for the meniscus pressure, p_m, and the length of the wetting layer, ℓ_{wet}.

6.4.1. *Meniscus pressure*

If the needle tip is large, the meniscus height is far from the ultra-thin-film thickness, ε, such that surface tension dominates and the meniscus is approximately parabolic; thus, we can relate the meniscus pressure to the length of the meniscus:

$$p_m \sim -\frac{h_{solid} - \varepsilon}{\ell_m{}^2}. \tag{6.12}$$

Since only ℓ_m is time-dependent on the right-hand side of this expression, we can write

$$p_m \sim -t^{-2a}. \tag{6.13}$$

6.4.2. *Growth of the wetting layer*

The growth of the wetting layer is governed by the collapse of the drop nearest the needle tip, i.e. the first drop (see figure 11). Following the work of Glasner & Witelski (2003), we derive an evolution equation for the pressure in the first drop using mass conservation:

$$\frac{dp_1}{dt} \sim \varepsilon^3 p_1{}^3 \left[\frac{\langle p \rangle - p_1}{\langle \ell \rangle} + \frac{p_m - p_1}{\ell_{wet}} \right]. \tag{6.14}$$

At early times, the meniscus pressure dominates, such that

$$\frac{dp_1}{dt} \sim \frac{1}{\ell_{wet}} p_1{}^3 p_m. \tag{6.15}$$

The wetting layer grows after the previous $(k - 1)$ first droplet collapses, at which time $\ell_{wet}{}^k \to \ell_{wet}{}^{k-1} + \langle \ell \rangle$. Before the collapse, the length of the wetting layer is roughly constant. Note that this assumption is true only if the droplet collapses much faster than the meniscus and the needle grow.

In the above differential equation, we can separate variables and integrate to find

$$p_1{}^{-2} \sim -\frac{1}{\ell_{wet}} t^{1-2a} + C. \tag{6.16}$$

As the droplet collapses, the pressure should diverge (since small droplets have high pressure). Thus, the droplet pressure can be written as

$$p_1 \sim \left[\frac{1}{\ell_{\mathrm{wet}}} (t_c - t)^{1-2a} \right]^{-1/2}, \tag{6.17}$$

where t_c is the time period for droplet collapse of the kth first drop. Note that t here is measured starting when the previous first drop $(k-1)$ collapses; thus, at $t = 0$, the kth drop should have the same pressure as a typical drop, i.e. $p_1(t = 0) = \langle p \rangle$, such that

$$t_c \sim \left(\ell_{\mathrm{wet}} \langle p \rangle^{-2} \right)^{1/(1-2a)}. \tag{6.18}$$

Each time a droplet collapses, the wetting layer grows in discrete steps. This discrete growth can be approximated over many steps by a continuous process:

$$\frac{\mathrm{d}\ell_{\mathrm{wet}}}{\mathrm{d}t} \sim \frac{\langle \ell \rangle}{t_c}. \tag{6.19}$$

Far away from the needle tip, the dynamics are governed by coarsening effects alone such that the typical drop spacing scales as $\langle \ell \rangle \sim t^{2/5}$, and pressure scales as $\langle p \rangle \sim t^{-1/5}$ (see Glasner & Witelski 2003). Combining these scalings with (6.13), (6.18), and (6.19) gives

$$\frac{\mathrm{d}\ell_{\mathrm{wet}}}{\mathrm{d}t} \sim \langle \ell \rangle \left(\ell_{\mathrm{wet}}^{-1} \langle p \rangle^2 \right)^{1/(1-2a)}. \tag{6.20}$$

Separating variables and integrating gives a wetting layer that grows as

$$\ell_{\mathrm{wet}} \sim t^{(5-14a)/(10-10a)}. \tag{6.21}$$

6.4.3. *Needle growth*

Now that scalings for p_m and ℓ_{wet} are known, the flow rate in (6.11) becomes

$$q_{\mathrm{wet}} \sim -t^{-(5+6a-20a^2)/(10-10a)}. \tag{6.22}$$

Note that q_{wet} is negative since the flux moves in the negative x-direction. We now return to (6.3), and substitute the scalings for the needle velocity (6.4), meniscus volume (6.6), and flux (6.22), which gives

$$t^{-a-b} + t^{a-1} \sim t^{-(5+6a-20a^2)/(10-10a)}. \tag{6.23}$$

All terms balance when $a \approx 0.29$ and $b \approx 0.42$, such that the needle velocity scales like $v_{tip} \sim t^{-0.71}$. Finally, integrating once in time gives a needle length which scales as

$$\ell_{needle} \sim t^{0.29}. \tag{6.24}$$

This scaling is confirmed in simulations, in which large values of h_{solid} lead to growth exponents that approach 0.29, as shown in figure 12.

7. Discussion

To examine consistency between simulations and experiments, we assume that the transport parameter scales as $\alpha \sim H_{Alq_3}^{-2}$. Strictly speaking $\alpha \sim H_0^{-2}$, where H_0 (the initial thickness of the fluid mixture) can differ from H_{Alq_3} due to the addition of methanol. All other parameters in α are collected as a fitting parameter. Nevertheless, when estimated using the material properties of pure methanol, α is order one
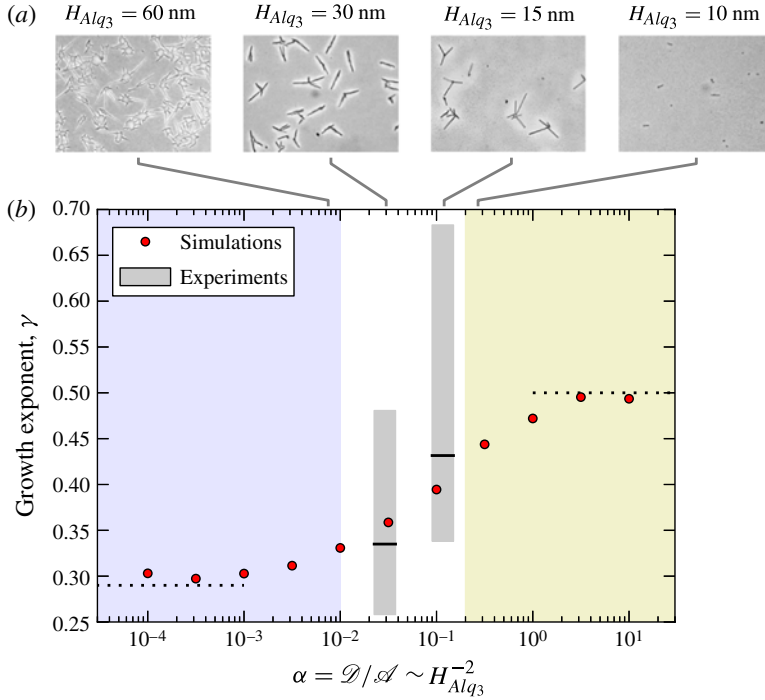
FIGURE 13. (Colour online) (*a*) Micrographs of needle growth for different thicknesses of Alq$_3$ films (from figure 3). (*b*) Growth exponents from simulations and experiments as a function of α. The two grey bars extend from the lower to upper quartile of the experimental data; while the line bisecting each bar marks the median of the data. The filled circles mark growth exponents from simulations. Experiments in the low-α regime produced inconsistent growth rates and those in the high-α regime failed to grow needles. The shaded region on the left indicates α values at which irregular crystalline morphologies are observed in the experiments. The shaded region on the right indicates film thicknesses that are sufficiently thin such that limited growth is observed and our continuum model breaks down.

(see table 1). The grey bars in figure 13 extend from the lower to upper quartile (i.e. the interquartile range) of the experimental data. The median of the experimental data, marked by the horizontal lines bisecting the grey bars, matches the trend predicted in simulations; i.e. the growth rate decreases for increasing film thickness. The large variations of γ in experiments (grey bars) arise from unpredictable nucleation behaviour, as discussed in §2. Although γ is plotted for a wide range of α-values, we only predict power-law behaviour at high and low α; the intermediate α-values probably constitute a cross-over regime between these asymptotic, power-law regimes.

In experiments, Alq$_3$ needles were typically >300 nm thick. Assuming that the thickness of thin-film mixture is roughly the same as the original Alq$_3$ film, needles will be more than an order of magnitude thicker than the thin film. Thus, experiments are in the large-h_{solid} regime and the growth exponent should approach 0.29 for small values of α, as depicted in figure 13.

While available experimental data are consistent with our scaling and numerics, the α-range in the experimental data presented in figure 13 is quite limited. Smaller α-values, attained with thicker Alq$_3$ films, produced crystals with a tapered (as opposed

	Low α (coarsening)	High α (diffusion)
Small needles	$\ell_{needle} \sim t^{2/5}$	$\ell_{needle} \sim t^{1/2}$
Large needles	$\ell_{needle} \sim t^{0.29}$	

TABLE 2. Summary of scaling laws in various growth regimes.

to rectangular) shape and highly-irregular growth rates (see left-most micrograph in figure 13a). In the high-α limit (thinner films), transport slowed dramatically and failed to produce needles reliably (see right-most micrograph in figure 13a). These issues prevented us from drawing a complete picture of the α-dependence. Other material/solvent/substrate combinations should be investigated to explore both lower and higher α-values.

In order to integrate single-crystal organic semiconductors into practical (opto)electronic devices, a physical understanding of crystal growth mechanisms in thin films is essential. In this paper, we have investigated the growth of single-crystal needles of Alq_3 from amorphous Alq_3 films annealed in methanol vapour. We developed a physical model describing solidification from thin-film liquid mixtures, along with a set of scaling laws that provide physical insight into the growth behaviour observed in numerical simulations.

In experiments, we annealed thin, amorphous films of Alq_3 in solvent vapour to promote needle growth, and captured real-time images of the growth process. Upon solvent-vapour annealing, the initially-uniform Alq_3 film formed drops and nucleated crystal needles. Needle growth exhibited a power-law behaviour, with the needle length scaling as $\ell_{needle} \sim t^{\gamma}$.

The governing equations were rescaled to produce a dimensionless transport coefficient, α, which relates diffusion to coarsening. For high α-values (diffusion-dominated regime), the needle length scaled as $\ell_{needle} \sim t^{1/2}$; this growth matches the theory of one-dimensional, diffusion-dominated solidification. For low α-values (coarsening-dominated regime), there were two sub-regimes: (i) small needles (i.e. $h_{solid} \lesssim \langle h_{drop} \rangle$) with needle lengths scaling as $\ell_{needle} \sim t^{2/5}$, and (ii) large needles (i.e. $h_{solid} \gg \langle h_{drop} \rangle$), with $\ell_{needle} \sim t^{0.29}$. Needle growth in these low α-regimes was dominated by fluid flux driven by droplet collapse, i.e. coarsening. These growth regimes are summarized in table 2. In order to test the validity of this analysis, we varied the thickness of the Alq_3 film, H_{Alq_3}, since $\alpha \sim H_0^{-2} \sim H_{Alq_3}^{-2}$. The measured growth exponents were consistent with the predicted range, and increased with increasing α, as predicted by the model.

Although these experiments were conducted on a single system, Alq_3–methanol–glass, the results should be applicable to many molecule–solvent–substrate systems. In particular, the behaviour of the system is governed by a set of dimensionless parameters, primarily α, which could be tuned using different molecules, solvents, and substrates. While our system falls primarily in the cross-over between coarsening-dominated and diffusion-dominated regimes, other material combinations should be investigated to shed light on the high- and low-α limits.

REFERENCES

BALLUFFI, R. W., ALLEN, S. M. & CARTER, W. C. 2005 *Kinetics of Materials*, 1st edn. Wiley-Interscience.

BECERRIL, H. A., ROBERTS, M. E., LIU, Z. H., LOCKLIN, J. & BAO, Z. N. 2008 High-performance organic thin-film transistors through solution-sheared deposition of small-molecule organic semiconductors. *Adv. Mater.* **20** (13), 2588–2594.

BECKER, J., GRUN, G., SEEMANN, R., MANTZ, H., JACOBS, K., MECKE, K. R. & BLOSSEY, R. 2003 Complex dewetting scenarios captured by thin-film models. *Nature Mater.* **2** (1), 59–63.

BOLLINNE, C., CUENOT, S., NYSTEN, B. & JONAS, A. M. 2003 Spinodal-like dewetting of thermodynamically-stable thin polymer films. *Eur. Phys. J.* E **12** (3), 389–395.

BRINKMANN, M., WITTMANN, J. C., CHAUMONT, C. & ANDRÈ, J. J. 1997 Effects of solvent on the morphology and crystalline structure of lithium phthalocyanine thin films and powders. *Thin Solid Films* **292** (1–2), 192–203.

CHEN, W., PENG, Q. & LI, Y. 2008 Alq(3) nanorods: promising building blocks for optical devices. *Adv. Mater.* **20** (14), 2747–2750.

COOK, B. P., BERTOZZI, A. L. & HOSOI, A. E. 2008 Shock solutions for particle–laden thin films. *SIAM J. Appl. Maths* **68** (3), 760–783.

CRANK, J. 1975 *Mathematics of Diffusion*. Clarendon.

CRASTER, R. V. & MATAR, O. K. 2009 Dynamics and stability of thin liquid films. *Rev. Mod. Phys.* **81** (3), 1131–1198.

DICKEY, K. C., ANTHONY, J. E. & LOO, Y. L. 2006 Improving organic thin-film transistor performance through solvent-vapour annealing of solution-processable triethylsilylethynyl anthradithiophene. *Adv. Mater.* **18** (13), 1721–1726.

GLASNER, K. B. & WITELSKI, T. P. 2003 Coarsening dynamics of dewetting films. *Phys. Rev.* E **67** (1, Part 2), 016302.

GLASNER, K. B. & WITELSKI, T. P. 2005 Collision versus collapse of droplets in coarsening of dewetting thin films. *Physica* D **209** (1–4), 80–104.

GOMBA, J. M. & HOMSY, G. M. 2009 Analytical solutions for partially wetting two-dimensional droplets. *Langmuir* **25** (10), 5684–5691.

GOTZE, W. & VOIGTMANN, T. 2003 Effect of composition changes on the structural relaxation of a binary mixture. *Phys. Rev.* E **67** (2), 021502.

GRANASY, L., PUSZTAI, T., BORZSONYI, T., WARREN, J. A. & DOUGLAS, J. F. 2004 A general mechanism of polycrystalline growth. *Nature Mater.* **3** (9), 645–650.

ISHII, Y., SHIMADA, T., OKAZAKI, N. & HASEGAWA, T. 2007 Wetting-dewetting oscillations of liquid films during solution-mediated vacuum deposition of rubrene. *Langmuir* **23** (12), 6864–6868.

ISRAELACHVILI, J. N. 1991 *Intermolecular and Surface Forces*, 2nd edn. Academic.

KAO, J. C. T., GOLOVIN, A. A. & DAVIS, S. H. 2006 Rupture of thin films with resonant substrate patterning. *J. Colloid Interface Sci.* **303** (2), 532–545.

LANGER, J. S. 1980 Instabilities and pattern-formation in crystal-growth. *Rev. Mod. Phys.* **52** (1), 1–28.

LEE, S., YOO, P., KWON, S. & LEE, H. 2004 Solvent-driven dewetting and rim instability. *J. Chem. Phys.* **121**, 4346.

LIU, S., WANG, W. M., BRISENO, A. L., MANNSFELD, S. C. B. & BAO, Z. 2009 Controlled deposition of crystalline organic semiconductors for field-effect-transistor applications. *Adv. Mater* **21** (12), 1217–1232.

DE LUCA, G., LISCIO, A., MACCAGNANI, P., NOLDE, F., PALERMO, V., MLLEN, K. & SAMORÏ, P. 2007 Nucleation-governed reversible self-assembly of an organic semiconductor at surfaces: long-range mass transport forming giant functional fibres. *Adv. Funct. Mater.* **17** (18), 3791–3798.

DE LUCA, G., LISCIO, A., NOLDE, F., SCOLARO, L. M., PALERMO, V., MULLEN, K. & SAMORI, P. 2008 Self-assembly of discotic molecules into mesoscopic crystals by solvent-vapour annealing. *Soft Matt.* **4** (10), 2064–2070.

MASCARO, D. J., THOMPSON, M. E., SMITH, H. I. & BULOVIC, V. 2005 Forming oriented organic crystals from amorphous thin films on patterned substrates via solvent-vapour annealing. *Organic Electron.* **6** (5–6), 211–220.

MILLER, S., FANCHINI, G., LIN, Y. Y., LI, C., CHEN, C. W., SU, W. F. & CHHOWALLA, M. 2008 Investigation of nanoscale morphological changes in organic photovoltaics during solvent vapour annealing. *J. Mater. Chem.* **18** (3), 306–312.

NÁRAIGH, L. & THIFFEAULT, J. 2007 Dynamical effects and phase separation in cooled binary fluid films. *Phys. Rev.* E **76** (3), 035303.

NARAIGH, L. O. & THIFFEAULT, J. 2010 Nonlinear dynamics of phase separation in thin films. *Nonlinearity* **23** (7), 1559–1583.

ORON, A., DAVIS, S. H. & BANKOFF, S. G. 1997 Long-scale evolution of thin liquid films. *Rev. Mod. Phys.* **69** (3), 931–980.

PRESS, W. H., TEUKOLSKY, S. A., VETTERLING, W. T. & FLANNERY, B. P. 1992 *Numerical Recipes in C: the Art of Scientific Computing*. Cambridge University Press.

RABANI, E., REICHMAN, D. R., GEISSLER, P. L. & BRUS, L. E. 2003 Drying-mediated self-assembly of nanoparticles. *Nature* **426** (6964), 271–274.

SEARS, J. K. & DARBY, J. R. 1982 *Technology of Plasticizers*. John Wiley & Sons.

SHARMA, A. 1993 Relationship of thin film stability and morphology to macroscopic parameters of wetting in the apolar and polar systems. *Langmuir* **9** (3), 861–869.

STAROV, V. & VELARDE, M. 2009 Surface forces and wetting phenomena. *J. Phys.: Condens. Matter* **21** (46), 464121.

TELETZKE, G. F., DAVIS, H. T. & SCRIVEN, L. E. 1988 Wetting hydrodynamics. *Rev. Phys. Appl.* **23** (6), 989–1007.

THIELE, U. 2011 Note on thin film equations for solutions and suspensions. *Eur. Phys. J.-Special Topics* **197** (1), 213–220.

TIAN, X., FEI, J., PI, Z., YANG, C., LUO, D., PEI, F. & ZHANG, L. 2006 Selective temperature physical vapour deposition route to tri(8-hydroquinoline)aluminum nanowires, nanowalls, nanoclusters and micro-spherical chains. *Solid State Commun.* **138** (10–11), 530–533.

VALLI, A. M. P., CAREY, G. F. & COUTINHO, A. L. G. A. 2005 Control strategies for time step selection in finite element simulation of incompressible flows and coupled reaction-convection-diffusion processes. *Intl J. Numer. Meth. Fluids* **47** (3), 201–231.

WETTLAUFER, J. S. & WORSTER, M. G. 2006 Premelting dynamics. *Annu. Rev. Fluid Mech.* **38**, 427–452.

XU, L., SHI, T. & AN, L. 2008 The dewetting dynamics of the polymer thin film by solvent annealing. *J. Chem. Phys.* **129**, 044904.

YU, T. S. 2011 Solidification in a thin liquid film: growing Alq_3 needles via methanol-vapour annealing. PhD thesis, MIT.

ZHOU, J. J., DUPUY, B., BERTOZZI, A. L. & HOSOI, A. E. 2005 Theory for shock dynamics in particle–laden thin films. *Phys. Rev. Lett.* **94** (11), 117803.